WILEY | Hindawi

Research Article

Facile Synthesis and Electrochemical Analysis of Zn-Doped V$_2$O$_5$ Anode Materials for High-Rate Li Storage

Yong-Jin Jang, Hyungeun Seo ⓘ, and Jae-Hun Kim ⓘ

School of Materials Science and Engineering, Kookmin University, Seoul 02707, Republic of Korea

Correspondence should be addressed to Jae-Hun Kim; jaehunkim@kookmin.ac.kr

The surging demand for Li rechargeable batteries with high energy densities and rapid rate capability has propelled research on materials that can replace the conventional anode materials like graphite. Vanadium pentoxides (V$_2$O$_5$) have emerged as promising anode candidates owing to their excellent rate capability. Specifically, V$_2$O$_5$ allows the electrochemical prelithiation process, in which three Li-ions can be inserted to form Li$_3$V$_2$O$_5$, followed by reversible insertion and extraction of two Li-ions. Nevertheless, the unsatisfactory Li-ion diffusion coefficients and electrical conductivities of these materials remain major drawbacks. Here, we propose a Zn-doped V$_2$O$_5$ anode, fabricated using a two-step sol–gel method, for high-rate Li-ion batteries. Zn was incorporated into V$_2$O$_5$ to enhance the Li-ion transport kinetics through the electrode. The crystal structure (orthorhombic) of Zn-doped V$_2$O$_5$ was identified by X-ray diffraction analysis, and the Zn doping was confirmed by X-ray photoelectron microscopy. The effect of Zn doping was thoroughly examined using various analytical methods, such as cyclic voltammetry and galvanostatic intermittent titration technique. The Zn-doped V$_2$O$_5$ electrode exhibited remarkable cycling durability, enduring for 1000 cycles, while retaining an enhanced capacity, even under a high rate of 2C.

1. Introduction

Li-ion batteries (LIBs) have undergone continuous development over several decades in response to market demand [1–4]. Carbon-based materials, particularly graphite, are extensively applied as anode materials in LIBs owing to their moderate capacity, strong cycling stability, and affordability [5–7]. However, their rate performance and capacity remain constrained because graphite can store Li-ions only through an intercalation mechanism [5–10]. Conversely, anode materials that rely on alloying mechanisms, such as Si and Sn, are also proposed owing to their high capacities and rapid rate characteristics [11–18]. However, structural degradation of these active components, caused by substantial volume changes during Li insertion and extraction, results in a subpar cycling performance [11–13]. Thus, developing novel materials suitable for extended usage and rapid charging applications is necessary.

Because of their outstanding chemical stability and cost-effectiveness, vanadium pentoxides (V$_2$O$_5$) are considered advantageous as electrode materials for LIBs [19–21]. How-

ever, the low diffusion coefficient of Li$^+$ ions and poor electrical conductivity of V$_2$O$_5$ limit its use in high-rate applications [22–24]. Several strategies such as structural and compositional manipulations, including cation doping, have been suggested to improve its rate performances [25–30]. Among these strategies, cation doping, which can enhance the intercalation and deintercalation kinetics of V$_2$O$_5$, has been widely explored [30–34]. To date, the feasibility of doping various cations such as Ni^{2+}, Mn^{2+}, Cu^{2+}, and Sn^{4+} has been investigated [30–33]. Li et al. prepared Sn-doped V$_2$O$_5$ microspheres using the solvothermal method [30]. Introducing Sn into V$_2$O$_5$ creates oxygen vacancies that facilitate the diffusion of Li-ions, leading to an enhanced capacity and rate performance. Similarly, Ni-V$_2$O$_5$ microspheres have been synthesized using a nickel-mediated polyol method followed by calcination [31]. Notably, these materials have been developed with a focus on fabricating cathodes for LIBs.

Recently, V$_2$O$_5$ has been repurposed as an anode material through an electrochemical prelithiation process, demonstrating impressive long-term cycling and excellent

rate capabilities [35]. The $Li_3V_2O_5$ material produced through the electrochemical prelithiation process has been further investigated [36–38]. Lan et al. exhibited the superior low-temperature performance of the full cell incorporating the $Li_3V_2O_5$ anode [36]. Ren et al. utilized the $Li_3V_2O_5$ material in Li-ion capacitors, demonstrating exceptional rate capability and remarkable cycling stability [37]. However, improving the limited Li-ion diffusion coefficients and electrical conductivities of V_2O_5 remains challenging. Hence, there is a need for a new method to address the issues associated with the existing V_2O_5 material and enhance its electrochemical performance as an anode for LIBs.

In this study, a novel method involving the introduction of Zn doping into V_2O_5 was proposed for the first time. The Zn doping effectively addressed issues in the original V_2O_5, thereby improving its electrochemical performance. To elucidate the reasons behind the improvement in electrochemical performance due to Zn doping and to confirm the presence of zinc doping, several structural and electrochemical analyses were conducted.

2. Experimental

2.1. Chemicals.
Vanadium pentoxide (V_2O_5, 99.6%) powder and ammonia solution (28-30%) were obtained from Sigma-Aldrich and utilized without additional refinement. Zinc nitrate hexahydrate ($Zn(NO_3)_2 \cdot 6H_2O$, 98%) was supplied by Samchun and utilized without additional purification.

2.2. Material Synthesis.
The Zn-doped V_2O_5 material (namely, the Zn-V_2O_5 sample) was synthesized using a two-step sol-gel procedure. Initially, 20 mmol of vanadium pentoxide and 1 mmol of zinc nitrate hexahydrate were dissolved in deionized (DI) water and agitated for 24 h to obtain a homogeneous solution. Subsequently, an ammonia solution was added into the prepared solution to adjust the pH to 8.5, and the resulting solution was stirred for an additional 24 h to create a uniform solution. Finally, the resulting solution was subjected to centrifugation and dried at 80°C for 12 h. Next, commercially available V_2O_5 powder without any modification (referred to as the V_2O_5 sample) was subjected to various analyses to serve as a reference.

2.3. Material Characterization.
To examine the crystal structures of the samples, the samples were analyzed by X-ray diffraction (XRD) using a Rigaku Ultima IV instrument. The morphology of the prepared specimens was assessed by field emission scanning electron microscopy (FE-SEM) using a JEOL 7500 microscope as well as by high-resolution transmission electron microscopy (HR-TEM) using a JEOL ARM-200F instrument. Additionally, X-ray photoelectron spectroscopy (XPS) was employed to analyze the chemical compositions of the samples.

2.4. Electrochemical Measurements.
The electrode fabrication process for all the samples was conducted as follows. First, the prepared active material (either V_2O_5 or Zn-V_2O_5 sample), a conducting agent (Super P), and a binder (polyvinylidene fluoride, PVDF, Kynar 2801), in a ratio of 60 : 30 : 10 by weight, were dissolved in N-methyl-2-pyrrolidone (NMP)
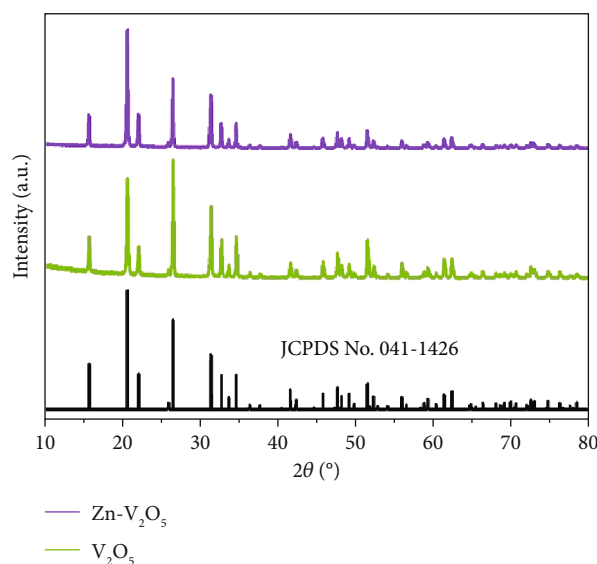

FIGURE 1: XRD patterns of the V_2O_5 and Zn-V_2O_5 samples.

solution. Next, the resulting slurry was applied onto a copper foil and subjected to vacuum drying at 120°C for a duration of 12 h (hereafter, the V_2O_5 and Zn-V_2O_5 electrodes are called as electrodes prepared from the V_2O_5 and Zn–V_2O_5 samples, respectively). Additionally, $Li_3V_2O_5$ and Zn–$Li_3V_2O_5$ electrodes were fabricated through lithiation of the V_2O_5 and Zn–V_2O_5 electrodes in a half cell operated at a current density of $0.1\,A\,g^{-1}$, respectively.

In the half-cell testing, a Li foil was used as the counter/reference electrode, and the prepared electrodes served as the working electrodes. The cell configuration included the prepared electrode, an electrolyte composed of 1 M $LiPF_6$ in a mixture of ethylene carbonate and diethyl carbonate (in a 3 : 7 volume ratio), an Li foil, and a polyethylene separator. Galvanostatic testing of the cells was conducted using a battery cycler (Basytec CTS-Lab) within a cutoff voltage range from 0.01 to 2.0 V (vs. Li^+/Li). All the operations were carried out under an inert atmosphere, specifically inside an Ar-filled glovebox.

To prepare an $LiNi_{0.8}Mn_{0.1}Co_{0.1}O_2$ cathode for full-cell tests, slurries were prepared by dissolving the active material ($LiNi_{0.8}Mn_{0.1}Co_{0.1}O_2$, 80% by weight), a conducting agent (Super P, 10% by weight), and a binder (PVDF, 10% by weight) in NMP. These slurries were then applied onto an Al-foil current collector. Following the coating process, the electrodes underwent compression and were subsequently dried in an oven at a temperature of 120°C for 12 h.

Cyclic voltammetry (CV) and electrochemical impedance spectroscopy (EIS) analyses were carried out using a potentiostat (BioLogic VSP). The CV measurements were conducted across a potential range of 0.01 to 2.0 V (vs. Li^+/Li) with varying scan rates of 0.2, 0.4, 0.6, 0.8, and $1.0\,mV\,s^{-1}$ at room temperature (25°C). Simultaneously, the EIS measurements were performed over a frequency range from 1 MHz to 0.1 Hz with an amplitude of 15 mV. To determine the Li-ion diffusion coefficients in the different materials, the galvanostatic intermittent titration technique (GITT) was employed. During the GITT test, charge and discharge cycles were executed within a potential range of
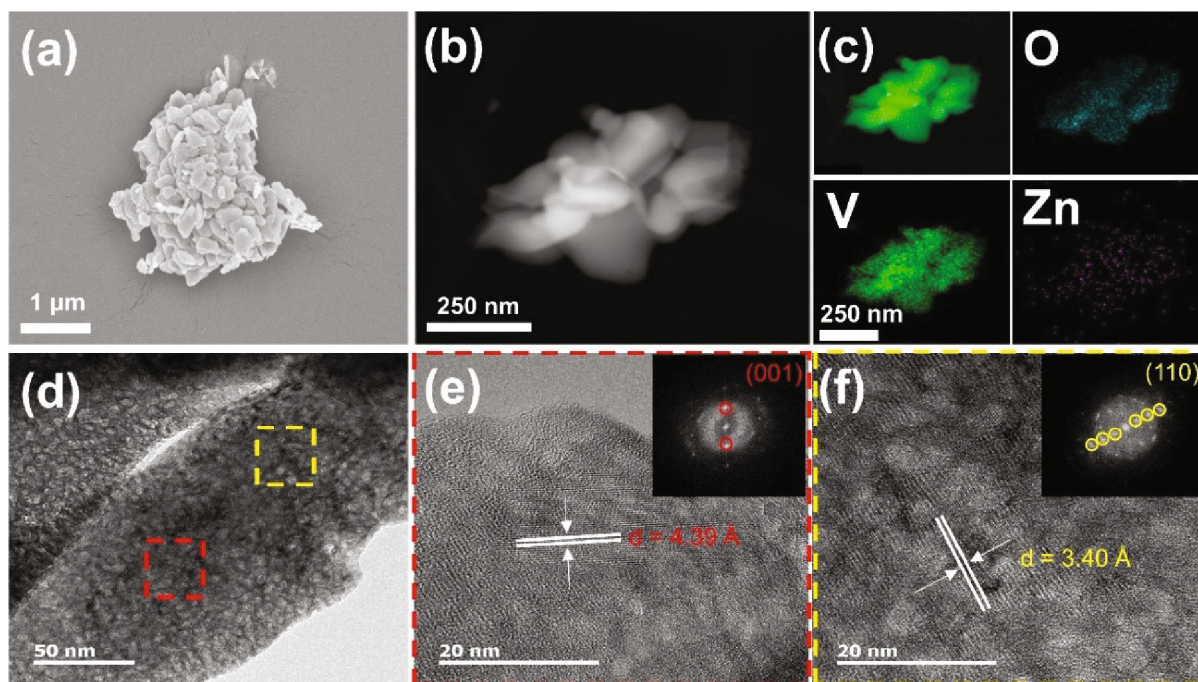
FIGURE 2: (a) FE-SEM, (b) TEM, (c) EDS elemental mapping images, (d) high-magnification TEM image, and (e, f) HR-TEM images with FFT patterns (inset) of the Zn-V_2O_5 sample.

0.01 V to 2.0 V (vs. Li$^+$/Li) using a pulse current of 0.1C (1C = 250 mAh g^{-1}) followed by a rest period of 3 h.

3. Results and Discussion

Figure 1 displays the XRD patterns of the V_2O_5 and Zn-V_2O_5 samples, incorporating reference values based on the standards established by the Joint Committee on Powder Diffraction Standards (JCPDS). In the pattern of the V_2O_5 sample (used as the precursor before the Zn doping), distinct peaks corresponding to the orthorhombic structure of V_2O_5 are observed (JCPDS No. 041-1426) [39]. The same peaks, which correspond to the orthorhombic structure of V_2O_5, are visible in the XRD profile of the Zn-V_2O_5 sample, suggesting that the orthorhombic structure of V_2O_5 is preserved even after the introduction of Zn. Furthermore, the obtained XRD patterns were magnified to investigate whether Zn doping could impact the cell parameters. The corresponding results are illustrated in Figure S1. In contrast to the V_2O_5 sample, the (001) and (110) reflections in the Zn-V_2O_5 sample exhibited a slight shift towards a lower angle. This indicates an expanded V_2O_5 lattice, attributed to the larger radius of Zn^{2+} (0.74 Å) compared to V^{5+} (0.68 Å). These findings suggest the incorporation of Zn^{2+} ions into the crystal structure of V_2O_5. The particle size of both samples from the XRD results based on the Debye-Scherrer equation can be calculated, and the results are shown in Table S1.

The Zn-V_2O_5 sample was analyzed using multiple characterization methods to gain insights into its morphology. Figure S2 displays the FE-SEM image of the V_2O_5 sample, corresponding to the typical FE-SEM image of a commercial V_2O_5 sample [40]. Figure 2(a) exhibits the FE-SEM image of the Zn-V_2O_5, showing aggregation of the

primary particles into a secondary particle. Figure 2(b) shows the TEM image with the energy dispersive spectroscopy (EDS) results (Figure 2(c)) of the Zn–V_2O_5 sample. The EDS graph is illustrated in Figure S3. Based on the EDS analysis results, it is confirmed that the V and O elements are uniformly distributed throughout the entire particle. Additionally, trace amounts of Zn (0.63 at%) are also detected, indicating the successful incorporation of Zn in this sample. Figure 2(d) presents the HR-TEM images, and Figures 2(e) and 2(f) show the fast Fourier transform (FFT) patterns of the samples. The measured lattice spacing of the crystallites is 3.40 and 4.39 Å, corresponding to the (110) and (001) reflections of the orthorhombic structure of V_2O_5, respectively [41]. The particle size distribution from the TEM images was obtained, and the results are given in Figure S4.

Subsequently, XPS analyses were conducted to discern the distinct chemical states of the V_2O_5 and Zn-V_2O_5 samples. Figure 3(a) displays the survey spectra of the V_2O_5 and Zn-V_2O_5 samples, and Figure 3(b) shows the Zn 2p core-level spectra of both the samples. No discernible peaks are visible in the spectrum of the undoped sample, whereas distinct peaks corresponding to ZnO (at 1022.1 and 1045.6 eV) appear in the spectrum of the Zn-doped sample [42, 43]. Figures 3(c) and 3(d) depict the V 2p$_{3/2}$ core-level spectra of the V_2O_5 and Zn-V_2O_5 samples, respectively, with deconvoluted profiles, and the corresponding areal ratios are presented in Table 1. The V 2p$_{3/2}$ spectra can be separated into two peaks corresponding to the V^{5+} (at 517.0 eV) and V^{4+} (at 515.7 eV) states [44, 45]. For the undoped sample, the determined areal ratios of V^{5+} and V^{4+} are 97.3% and 2.7%, respectively. By contrast, in the Zn-doped sample, the areal ratio of V^{5+} decreases from 97.3% to 94.2%, while
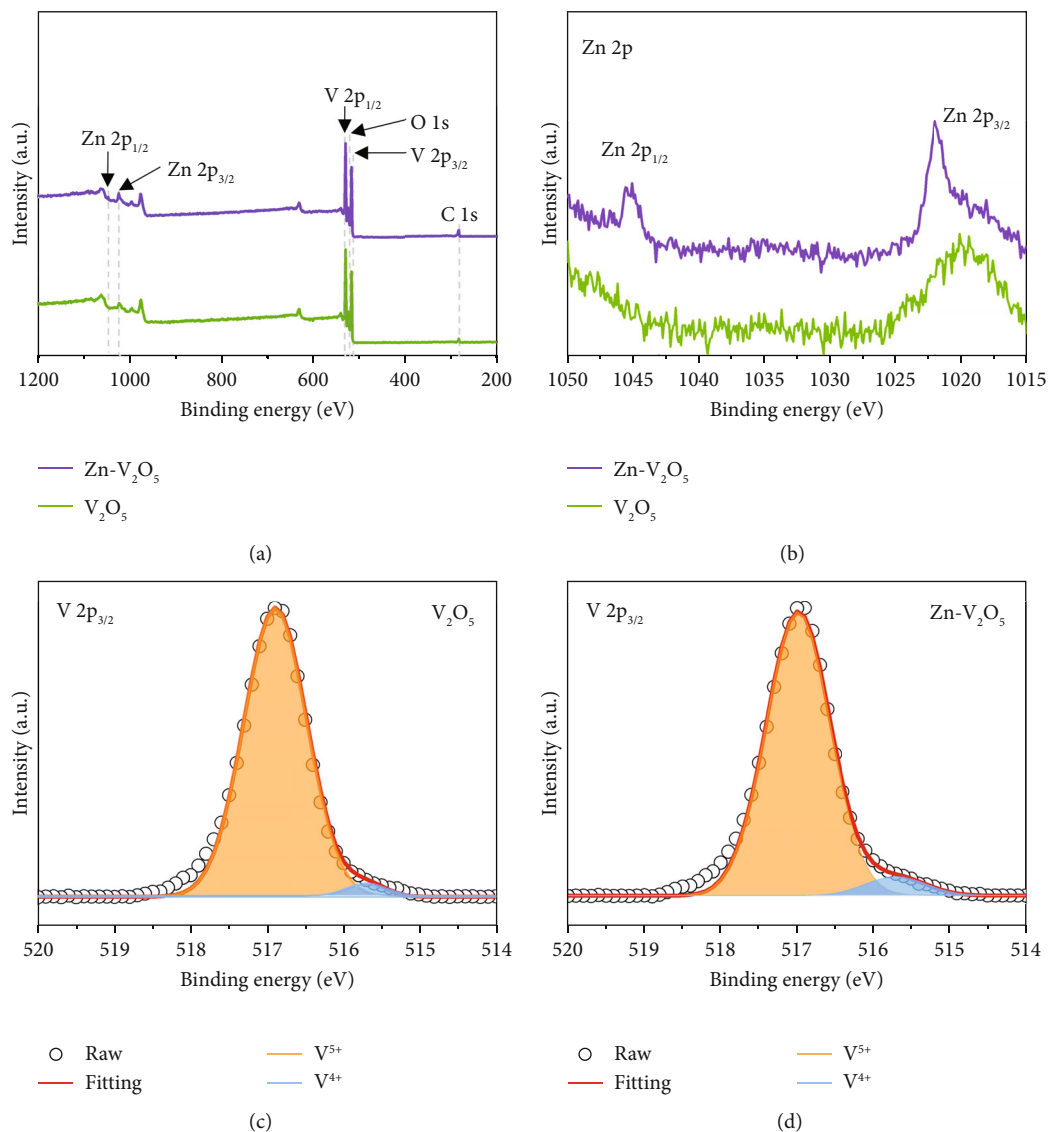
FIGURE 3: XPS spectra of the V_2O_5 and Zn-V_2O_5 samples: (a) survey spectrum, (b) Zn 2p core-level spectra of both the samples, and V $2p_{3/2}$ core-level spectra of (c) V_2O_5 and (d) Zn-V_2O_5.

TABLE 1: Abundance ratio for the V valence states observed in the V $2p_{3/2}$ XPS spectra of the V_2O_5 and Zn-V_2O_5 samples.

Sample	Peak indexing	V^{5+}	V^{4+}
V_2O_5	Peak (eV)	516.9	515.7
	Area (%)	97.3	2.7
Zn-V_2O_5	Peak (eV)	517	515.7
	Area (%)	94.2	5.8

that of V^{4+} increases from 2.7% to 5.8%. Figure S5a and b shows the O 1s core-level spectra of the V_2O_5 and Zn-V_2O_5 samples, respectively, with deconvoluted profiles. The corresponding areal ratios for the V_2O_5 and Zn-V_2O_5 samples are shown in Table S2. The O 1s spectra can be distinguished into two peaks originating from the V^{5+} (529.9 eV) and V^{4+} (531.2 eV) states [45]. The deconvoluted O 1s spectra are similar to those of V $2p_{3/2}$ spectra shown in

Figure 3. Specifically, before the Zn doping, the areal ratios for V^{5+} and V^{4+} are 92.5% and 7.5%, respectively. By contrast, following the Zn doping, the areal ratio of V^{5+} decreases from 92.5% to 88.6%, while that of V^{4+} increases from 7.5% to 11.4%. The increased V^{4+}/V^{5+} ratio after zinc doping can be ascribed to the substitution of V^{5+} by Zn^{2+} ions, indicating the successful doping of Zn into V_2O_5. Moreover, the occupation of V^{5+} sites by Zn^{2+} leads to the formation of oxygen vacancies, creating rapid channels for Li^+ intercalation/extraction [30].

To assess the ability of the Zn-V_2O_5 sample to undergo electrochemical prelithiation to yield ω-$Li_3V_2O_5$, we conducted ex situ XRD measurements at a cutoff voltage of 1.9 V. Figure S6 presents the ex situ XRD patterns of the V_2O_5 and Zn-V_2O_5 electrodes discharged to 1.9 V at 0.1 A g^{-1}. Evidently, both the V_2O_5 and Zn-V_2O_5 electrodes exhibit identical peaks at approximately 38.16°, 44.42°, and 64.44°, corresponding to the (111), (200), and (220) crystal
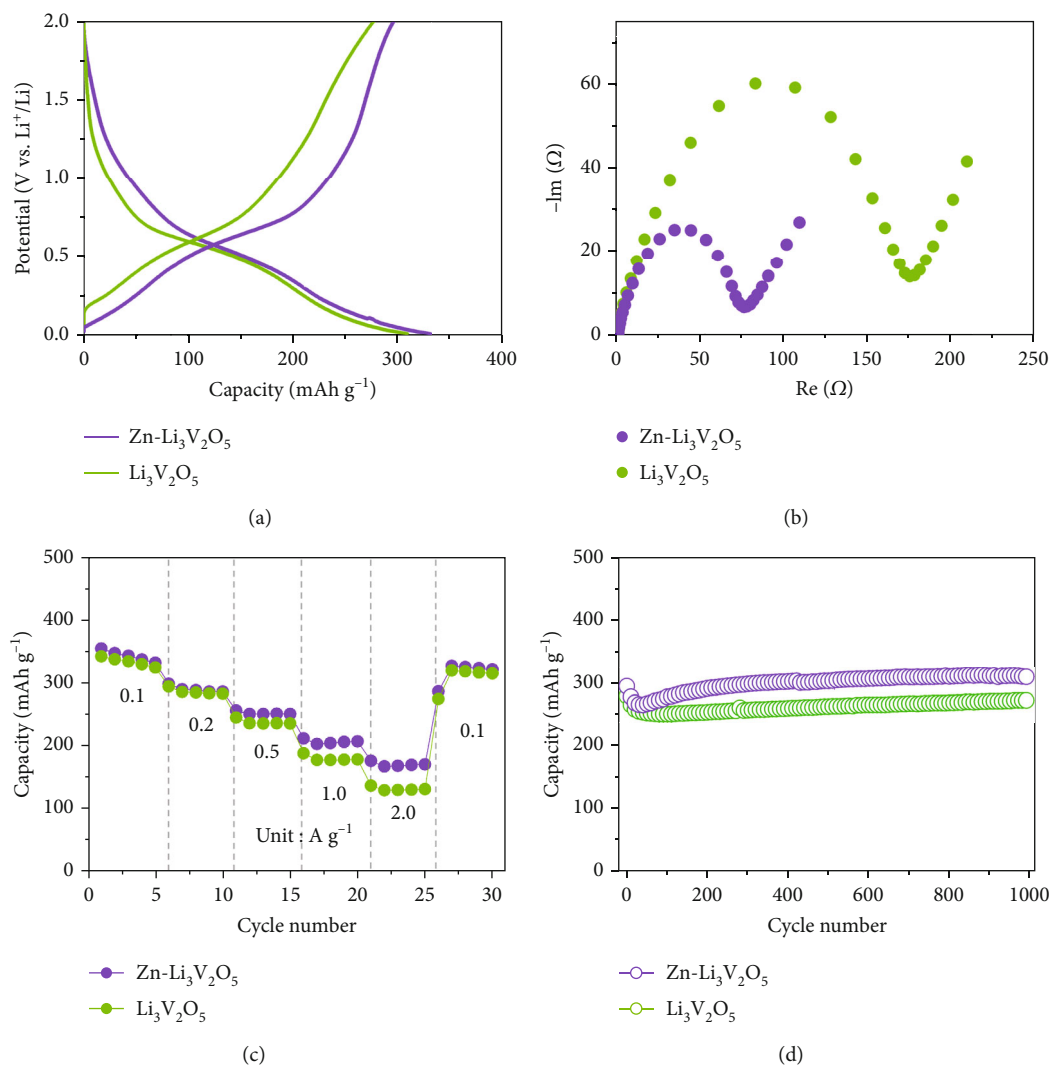
FIGURE 4: (a) Voltage profiles at a specific current of $500\,mA\,g^{-1}$, (b) Nyquist plots, (c) rate performance, and (d) cycling performance of the $Li_3V_2O_5$ and $Zn-Li_3V_2O_5$ electrodes at a specific current of $500\,mA\,g^{-1}$.

planes of ω-$Li_3V_2O_5$, respectively [35]. This result indicates that similar to V_2O_5, Zn–V_2O_5 can indeed undergo electrochemical prelithiation to form ω-$Li_3V_2O_5$.

Figure 4 presents the electrochemical properties of the $Li_3V_2O_5$ and $Zn-Li_3V_2O_5$ electrodes. The voltage profiles of these electrodes shown in Figure 4(a) indicate that for the $Li_3V_2O_5$ electrode, the initial discharge and charge capacities are 309.3 and $277.4\,mAh\,g^{-1}$, respectively, with an initial coulombic efficiency of 89.7%. Conversely, for the Zn-$Li_3V_2O_5$ electrode, the initial discharge and charge capacities at a 2C rate ($1C = 250\,mA\,g^{-1}$) are 321.4 and $298.1\,mAh\,g^{-1}$, respectively, with an initial coulombic efficiency of 92.8%. Notably, after the Zn doping, the capacities and initial coulombic efficiencies improved. Figure 4(b) illustrates the Nyquist plots of the $Li_3V_2O_5$ and $Zn-Li_3V_2O_5$ electrodes, indicating that the resistance of the $Zn-Li_3V_2O_5$ electrode is lower than that of the $Li_3V_2O_5$ electrode. This reduction in resistance can be attributed to the Zn doping-induced oxygen vacancies, which reduce the charge-transfer resistance [31]. Figure 4(c) compares the rate performances of

the $Li_3V_2O_5$ and $Zn-Li_3V_2O_5$ electrodes. Notably, the capacity of the $Zn-Li_3V_2O_5$ electrode surpasses that of the $Li_3V_2O_5$ electrode at various rates, and this improved rate capability can be assigned to the Zn doping effect. Lastly, Figure 4(d) shows the cycling performances of both the $Li_3V_2O_5$ and $Zn-Li_3V_2O_5$ electrodes at 2C. The $Zn-Li_3V_2O_5$ electrode consistently outperforms the $Li_3V_2O_5$ electrode in terms of capacity retention over extended cycling periods. Overall, the enhancement in the electrochemical characteristics of the Zn-V_2O_5 sample can be attributed to the oxygen vacancies created by the introduction of Zn. These vacancies increase the number of active sites available for the intercalation and deintercalation of the Li^+ ions [30, 31].

To assess the practical applicability of the proposed Zn-doped anode, a full cell was assembled using the $Zn-Li_3V_2O_5$ anode, which was prepared using the electrochemical lithiation method described earlier, and an $LiNi_{0.8}Co_{0.1}Mn_{0.1}O_2$ (NCM 811) cathode (Figure S7). Figure S7a shows the voltage profiles of the full cell subjected to cycling at a consistent current of $0.1\,A\,g^{-1}$ within a voltage range of 1.5 V
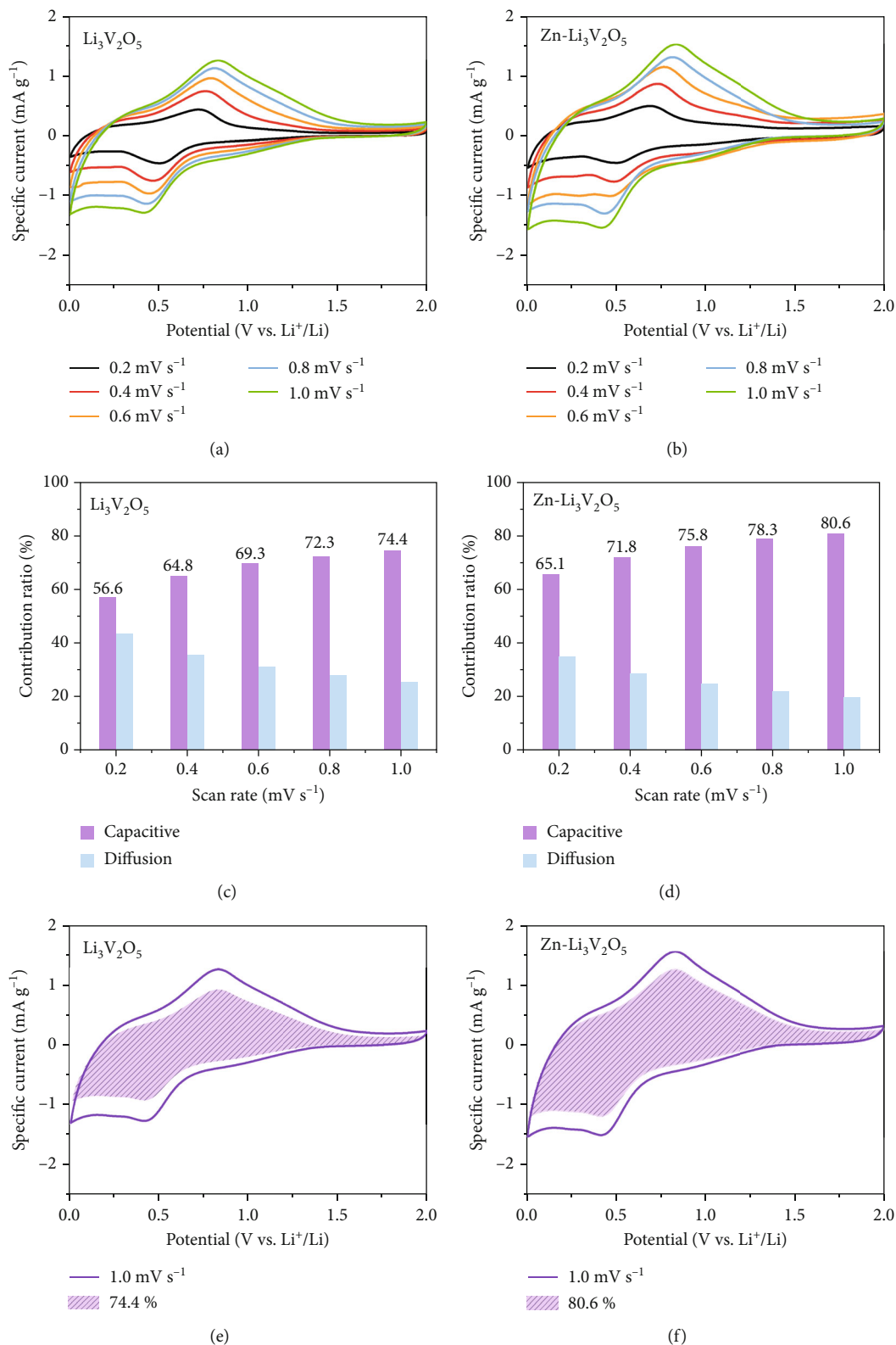
FIGURE 5: Kinetic analysis of the $Li_3V_2O_5$ and $Zn-Li_3V_2O_5$ electrodes: (a, b) CV curves recorded at different scan rates; (c, d) contribution ratios of the capacitive and diffusion reactions at different scan rates; (e, f) CV curves with capacitive contribution ratios at $1.0\,mV\,s^{-1}$.

to 3.9 V. Figure S7b shows the cycling performance of the full cell at a rate of $0.1\,A\,g^{-1}$, demonstrating its robust stability over 200 cycles without noticeable degradation.

To investigate the Li^+ storage mechanism of the $Li_3V_2O_5$ and $Zn-Li_3V_2O_5$ electrodes, we conducted CV measurements at different scan rates ranging from 0.2 to $1.0\,mV\,s^{-1}$.

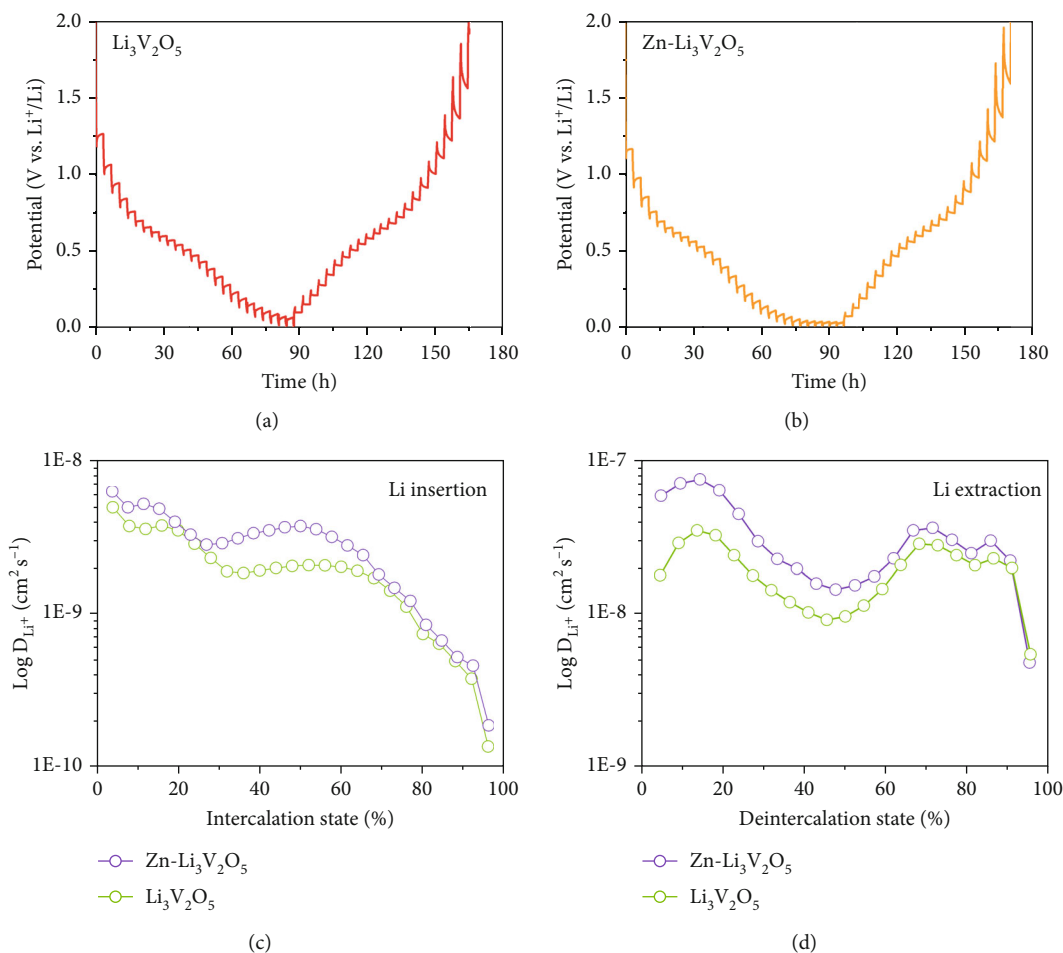FIGURE 6: (a, b) GITT curves of the $Li_3V_2O_5$ and Zn-$Li_3V_2O_5$ electrodes. (c, d) Li-ion diffusion coefficients calculated from GITT curves recorded during the Li insertion and extraction processes.

Figures 5(a) and 5(b) show the CV results of the $Li_3V_2O_5$ and Zn-$Li_3V_2O_5$ electrodes, respectively. The CV curves of both the electrodes exhibit distinct peaks at approximately 0.3–0.8 V (vs. Li^+/Li), which can be attributed to the processes of Li insertion and extraction [37]. Notably, the shapes and positions of these CV curves remain consistent, irrespective of the presence of the Zn dopants or variations in the scan rate. According to the power law, the relationship between peak current and scan rate can be expressed using the following equation [37, 46–48]:

$$I = av^b, \qquad (1)$$

where I is the peak current, a and b are constant parameters, and v is the scan rate. The Li^+ storage mechanisms can be elucidated by assessing the values of the parameter "b." Specifically, b approaching 0.5 implies that the Li^+ storage mechanism is predominantly governed by a diffusion-limited process. Conversely, a b value of 1.0 signifies that the Li^+ storage mechanism is entirely controlled by a capacitive process [46]. The computed b values, based on the CV curves displayed in Figures 5(a) and 5(b), are presented in Figure S8a and b for the $Li_3V_2O_5$ and Zn-$Li_3V_2O_5$ samples, respectively.

Evidently, the b values exhibited by the Zn–$Li_3V_2O_5$ electrode for both anodic and cathodic peaks are higher than that shown by the $Li_3V_2O_5$ electrode. This result suggests that unlike the reactions that occur in the $Li_3V_2O_5$ electrode, those in the Zn-$Li_3V_2O_5$ electrode are more likely controlled by a capacitive process.

Moreover, the peak current ($I = av^b$) originates from two different mechanisms, i.e., capacitive and diffusion-limited processes, as described in the following equation [47]:

$$I = k_1v + k_2v^{1/2}, \qquad (2)$$

where I is the peak current at a certain potential and k_1v and $k_2v^{1/2}$ represent the capacitive and diffusion-limited processes, respectively. The capacitive and diffusion contributions calculated based on the above equation at a scan rate of 0.2–1.0 mV s^{-1} for both the electrodes are shown in Figures 5(c) and 5(d). The capacitive contributions determined from the areal portions in the CV curves at 1.0 mV s^{-1} are displayed in Figures 5(e) and 5(f). In the $Li_3V_2O_5$ electrode, the capacitive contribution at a scan rate of 0.2 mV s^{-1} is 56.6%, which gradually increases to 74.4% at a scan rate of 1.0 mV s^{-1}. By contrast, the capacitive

contributions in the Zn-Li$_3$V$_2$O$_5$ electrode at scan rates of 0.2 and 1.0 mV s^{-1} are 65.1% and 80.6%, respectively, which are higher than those in the Li$_3$V$_2$O$_5$ electrode. This result implies that Zn-V$_2$O$_5$ is superior to V$_2$O$_5$ in terms of rapid Li$^+$ storage kinetics. The accelerated Li$^+$ storage kinetics observed in the Zn-V$_2$O$_5$ sample can be attributed to the creation of oxygen vacancies through the introduction of Zn. Presence of oxygen vacancies is advantageous for forming a more open structure, which facilitates easy penetration and movement of Li-ions [30, 31].

Additionally, we employed the GITT to analyze the Li-ion diffusion coefficients, and the corresponding results obtained for the Li$_3$V$_2$O$_5$ and Zn-Li$_3$V$_2$O$_5$ electrodes are shown in Figures 6(a) and 6(b), respectively. The Li-ion diffusion coefficient can be calculated using the following equation [49–52]:

$$D_{\mathrm{Li}} = \frac{4L^2}{\pi\tau}\left(\frac{\Delta E_{\mathrm{s}}}{\Delta E_{\mathrm{t}}}\right)^2, \tag{3}$$

where L, τ, ΔE_{s}, and ΔE_{t} denote the electrode thickness, pulse duration, steady-state voltage change, and total voltage change (eliminating iR drop), respectively. The Li-ion diffusion coefficients, determined from the GITT curves during the Li insertion and extraction processes, are illustrated in Figures 6(c) and 6(d). Specifically, during the Li insertion process, the average Li-ion diffusion coefficients for the Li$_3$V$_2$O$_5$ and Zn-Li$_3$V$_2$O$_5$ electrodes are computed as 2.03 and 2.81×10^{-9} cm^2 s^{-1}, respectively. Conversely, during the Li extraction process, the average Li-ion diffusion coefficients for the Li$_3$V$_2$O$_5$ and Zn-Li$_3$V$_2$O$_5$ electrodes decrease to 1.97 and 3.33×10^{-8} cm^2 s^{-1}, respectively. The observed high average Li-ion diffusion coefficients of the Zn–Li$_3$V$_2$O$_5$ electrode confirm that the Zn doping into V$_2$O$_5$ improved the Li$^+$ diffusion kinetics in the doped electrode. The electrochemical kinetic investigation results confirm the excellent capacitive behavior and high Li-ion diffusion coefficients of the Zn-V$_2$O$_5$ composite; these factors collectively enhance its rate performance as well as capacity.

4. Conclusions

In this study, we introduced, for the first time, the concept of doping Zn into V$_2$O$_5$ using a two-step sol-gel method. Zn doping into V$_2$O$_5$ was employed to enhance the conductivity and Li-ion diffusion rates of V$_2$O$_5$. Consequently, the electrochemical performance of V$_2$O$_5$ as an anode for LIBs was improved through zinc doping. The incorporation of Zn into V$_2$O$_5$ was verified using multiple analytical techniques, such as EDS and XPS. In addition, multiple structural and electrochemical analyses confirmed that Zn incorporation improved the Li$^+$ ion storage kinetics of V$_2$O$_5$, and the resultant Zn-V$_2$O$_5$ material consequently exhibited strong capacitive behavior. Lastly, these materials exhibited excellent cycling durability, sustaining their performance for over 1000 cycles at a high discharge rate of 2C, while delivering superior rate performances along with increased capacity compared to the V$_2$O$_5$ sample. The zinc

doping method can open up new possibilities for developing electrodes in high-power energy storage.

Data Availability

The data that supports the findings of this study are available from the corresponding author upon a reasonable request.

Conflicts of Interest

There are no conflicts to declare.

Acknowledgments

Supplementary Materials

Figure S1: enlarged XRD patterns of the Zn-V$_2$O$_5$ and V$_2$O$_5$ samples. Figure S2: FE-SEM image of the V$_2$O$_5$ sample. Figure S3: EDS results of the Zn-V$_2$O$_5$ sample. Figure S4: (a, c) TEM images of the V$_2$O$_5$ and Zn-V$_2$O$_5$ samples. (b, d) Particle size distribution plots obtained from the TEM images of the V$_2$O$_5$ and Zn-V$_2$O$_5$ samples. Figure S5: O 1s XPS core-level spectra for the (a) V$_2$O$_5$ and (b) Zn-V$_2$O$_5$ samples. Figure S6: *ex situ* XRD profiles of the V$_2$O$_5$ and Zn-V$_2$O$_5$ electrodes at a cutoff voltage of 1.9 V. Figure S7: (a) voltage profiles and (b) cycling performances of Zn-Li$_3$V$_2$O$_5$||NCM 811 full cell at 100 mA g^{-1}. Figure S8: b values calculated from the log (scan rate) vs. log (peak current) curves. Table S1: crystallite size calculation using the Debye-Scherrer equation. Table S2: abundance ratio for the O valence states observed in the O 1s XPS spectra of the V$_2$O$_5$ and Zn-V$_2$O$_5$ samples. (*Supplementary Materials*)

References

[1] B. Scrosati and J. Garche, "Lithium batteries: status, prospects and future," *Journal of Power Sources*, vol. 195, no. 9, pp. 2419–2430, 2010.

[2] H. Kim, G. Jeong, Y.-U. Kim, J.-H. Kim, C.-M. Park, and H.-J. Sohn, "Metallic anodes for next generation secondary batteries," *Chemical Society Reviews*, vol. 42, no. 23, pp. 9011–9034, 2013.

[3] Y. An, H. Fei, G. Zeng et al., "Green, scalable, and controllable fabrication of nanoporous silicon from commercial alloy precursors for high-energy lithium-ion batteries," *ACS Nano*, vol. 12, no. 5, pp. 4993–5002, 2018.

[4] Y. An, Y. Tian, C. Wei et al., "Scalable and physical synthesis of 2D silicon from bulk layered alloy for lithium-ion batteries and lithium metal batteries," *ACS Nano*, vol. 13, no. 12, pp. 13690–13701, 2019.

[5] M. Winter, J. O. Besenhard, M. E. Spahr, and P. Novák, "Insertion electrode materials for rechargeable lithium batteries," *Advanced Materials*, vol. 10, no. 10, pp. 725–763, 1998.

[6] H. Zhang, Y. Yang, D. Ren, L. Wang, and X. He, "Graphite as anode materials: fundamental mechanism, recent progress and

advances," *Energy Storage Materials*, vol. 36, pp. 147–170, 2021.

[7] C. Zhong, S. Weng, Z. Wang, C. Zhan, and X. Wang, "Kinetic limits and enhancement of graphite anode for fast-charging lithium-ion batteries," *Nano Energy*, vol. 117, article 108894, 2023.

[8] N. A. Kaskhedikar and J. Maier, "Lithium storage in carbon nanostructures," *Advanced Materials*, vol. 21, no. 25-26, pp. 2664–2680, 2009.

[9] D. Aurbach, B. Markovsky, I. Weissman, E. Levi, and Y. Ein-Eli, "On the correlation between surface chemistry and performance of graphite negative electrodes for Li ion batteries," *Electrochimica Acta*, vol. 45, no. 1-2, pp. 67–86, 1999.

[10] P. Yu, B. S. Haran, J. A. Ritter, R. E. White, and B. N. Popov, "Palladium-microencapsulated graphite as the negative electrode in Li-ion cells," *Journal of Power Sources*, vol. 91, no. 2, pp. 107–117, 2000.

[11] C.-M. Park, J.-H. Kim, H. Kim, and H.-J. Sohn, "Li-alloy based anode materials for Li secondary batteries," *Chemical Society Reviews*, vol. 39, no. 8, pp. 3115–3141, 2010.

[12] M. N. Obrovac and V. L. Chevrier, "Alloy negative electrodes for Li-ion batteries," *Chemical Reviews*, vol. 114, no. 23, pp. 11444–11502, 2014.

[13] U. Kasavajjula, C. Wang, and A. J. Appleby, "Nano- and bulk-silicon-based insertion anodes for lithium-ion secondary cells," *Journal of Power Sources*, vol. 163, no. 2, pp. 1003–1039, 2007.

[14] X. Chen, K. Gerasopoulos, J. Guo et al., "Virus-enabled silicon anode for lithium-ion batteries," *ACS Nano*, vol. 4, no. 9, pp. 5366–5372, 2010.

[15] H. K. Liu, Z. P. Guo, J. Z. Wang, and K. Konstantinov, "Si-based anode materials for lithium rechargeable batteries," *Journal of Materials Chemistry*, vol. 20, no. 45, pp. 10055–10057, 2010.

[16] M. Ashuri, Q. He, and L. L. Shaw, "Silicon as a potential anode material for Li-ion batteries: where size, geometry and structure matter," *Nanoscale*, vol. 8, no. 1, pp. 74–103, 2016.

[17] Q. Liu, Z. Cui, R. Zou, J. Zhang, K. Xu, and J. Hu, "Surface coating constraint induced anisotropic swelling of silicon in Si–Void@SiO_x nanowire anode for lithium-ion batteries," *Small*, vol. 13, no. 13, article 1603754, 2017.

[18] H. Lee, A. N. Preman, T. N. Vo, J.-H. Lee, I. T. Kim, and S.-k. Ahn, "In situ crosslinkable acrylic random copolymer binders for silicon anodes in lithium-ion batteries," *International Journal of Energy Research*, vol. 46, no. 9, pp. 12565–12578, 2022.

[19] J. Yao, Y. Li, R. C. Massé, E. Uchaker, and G. Cao, "Revitalized interest in vanadium pentoxide as cathode material for lithium-ion batteries and beyond," *Energy Storage Materials*, vol. 11, pp. 205–259, 2018.

[20] D. McNulty, D. N. Buckley, and C. O'Dwyer, "Synthesis and electrochemical properties of vanadium oxide materials and structures as Li-ion battery positive electrodes," *Journal of Power Sources*, vol. 267, pp. 831–873, 2014.

[21] Y. Yue and H. Liang, "Micro- and nano-structured vanadium pentoxide (V_2O_5) for electrodes of lithium-ion batteries," *Advanced Energy Materials*, vol. 7, no. 17, article 1602545, 2017.

[22] T. Watanabe, Y. Ikeda, T. Ono et al., "Characterization of vanadium oxide sol as a starting material for high rate intercalation cathodes," *Solid State Ionics*, vol. 151, no. 1-4, pp. 313–320, 2002.

[23] J. Muster, G. T. Kim, V. Krstić et al., "Electrical transport through individual vanadium pentoxide nanowires," *Advanced Materials*, vol. 12, no. 6, pp. 420–424, 2000.

[24] Y. Sun, L. Zhang, S. Wang, I. Lieberwirth, Y. Yu, and C. Chen, "Walnut-like vanadium oxide film with high rate performance as a cathode material for rechargeable lithium batteries," *Journal of Power Sources*, vol. 228, pp. 7–13, 2013.

[25] Y. Liu, M. Clark, Q. Zhang et al., "V_2O_5 nano-electrodes with high power and energy densities for thin film Li-ion batteries," *Advanced Energy Materials*, vol. 1, no. 2, pp. 194–202, 2011.

[26] J. Shin, H. Jung, Y. Kim, and J. Kim, "Carbon-coated V_2O_5 nanoparticles with enhanced electrochemical performance as a cathode material for lithium ion batteries," *Journal of Alloys and Compounds*, vol. 589, pp. 322–329, 2014.

[27] H. Song, C. Liu, C. Zhang, and G. Cao, "Self-doped V^{4+}– V_2O_5 nanoflake for 2 Li-ion intercalation with enhanced rate and cycling performance," *Nano Energy*, vol. 22, pp. 1–10, 2016.

[28] X.-F. Zhang, K.-X. Wang, X. Wei, and J.-S. Chen, "Carbon-coated V_2O_5 nanocrystals as high performance cathode material for lithium ion batteries," *Chemistry of Materials*, vol. 23, no. 24, pp. 5290–5292, 2011.

[29] J. Shao, X. Li, Z. Wan et al., "Low-cost synthesis of hierarchical V_2O_5 microspheres as high-performance cathode for lithium-ion batteries," *ACS Applied Materials & Interfaces*, vol. 5, no. 16, pp. 7671–7675, 2013.

[30] Z. Li, C. Zhang, C. Liu et al., "Enhanced electrochemical properties of Sn-doped V_2O_5 as a cathode material for lithium ion batteries," *Electrochimica Acta*, vol. 222, pp. 1831–1838, 2016.

[31] Y.-Z. Zheng, H. Ding, E. Uchaker et al., "Nickel-mediated polyol synthesis of hierarchical V_2O_5 hollow microspheres with enhanced lithium storage properties," *Journal of Materials Chemistry A*, vol. 3, no. 5, pp. 1979–1985, 2015.

[32] H. Zeng, D. Liu, Y. Zhang et al., "Nanostructured Mn-doped V_2O_5 cathode material fabricated from layered vanadium jarosite," *Chemistry of Materials*, vol. 27, no. 21, pp. 7331–7336, 2015.

[33] H. Yu, X. Rui, H. Tan et al., "Cu doped V_2O_5 flowers as cathode material for high-performance lithium ion batteries," *Nanoscale*, vol. 5, no. 11, pp. 4937–4943, 2013.

[34] D. Vernardou, I. Marathianou, N. Katsarakis et al., "Capacitive behavior of Ag doped V_2O_5 grown by aerosol assisted chemical vapour deposition," *Electrochimica Acta*, vol. 196, pp. 294–299, 2016.

[35] H. Liu, Z. Zhu, Q. Yan et al., "A disordered rock salt anode for fast-charging lithium-ion batteries," *Nature*, vol. 585, no. 7823, pp. 63–67, 2020.

[36] X. Lan, L. Wang, L. Yu, Y. Li, and X. Hu, "Synergy of highly reversible ω-$Li_3V_2O_5$ anodes and fluorine-containing additive electrolytes promises low-temperature-tolerant Li-ion batteries," *ACS Materials Letters*, vol. 3, no. 9, pp. 1394–1401, 2021.

[37] Z. Ren, S. Yu, T. Yao, T. Xu, J. He, and L. Shen, "Crystal phase and morphology engineering of ω-$Li_3V_2O_5$ nanospheres for high-rate lithium-ion capacitors," *Journal of Materials Chemistry A*, vol. 11, no. 2, pp. 621–629, 2023.

[38] Z. Wang, S. Yuan, X. Tang et al., "Enhanced Li-ion migration behavior in $Li_3V_2O_5$ rock-salt anode via stepwise lattice tailoring," *Energy Storage Materials*, vol. 54, pp. 284–293, 2023.

[39] F. Haaß, A. H. Adams, T. Buhrmester, G. Schimanke, M. Martin, and H. Fuess, "X-Ray absorption and X-ray diffraction studies on molybdenum doped vanadium pentoxide," *Physical Chemistry Chemical Physics*, vol. 5, no. 19, pp. 4317–4324, 2003.

[40] Y. Chen, C. Chen, W. Chen, H. Liu, and J. Zhu, "Influence of thermal-decomposition temperatures on structures and properties of V_2O_5 as cathode materials for lithium ion battery," *Progress in Natural Science: Materials International*, vol. 25, no. 1, pp. 42–46, 2015.

[41] Y. Zhang, Y. Wang, Z. Xiong et al., "V_2O_5 nanowire composite paper as a high-performance lithium-ion battery cathode," *ACS Omega*, vol. 2, no. 3, pp. 793–799, 2017.

[42] G. Qu, G. Fan, M. Zhou et al., "Graphene-modified ZnO nanostructures for low-temperature NO_2 sensing," *ACS Omega*, vol. 4, no. 2, pp. 4221–4232, 2019.

[43] S.-S. Li and Y.-K. Su, "Improvement of the performance in Cr-doped ZnO memory devices via control of oxygen defects," *RSC Advances*, vol. 9, no. 6, pp. 2941–2947, 2019.

[44] M. J. Powell, I. J. Godfrey, R. Quesada-Cabrera et al., "Qualitative XANES and XPS analysis of substrate effects in VO_2 thin films: a route to improving chemical vapor deposition synthetic methods?," *The Journal of Physical Chemistry C*, vol. 121, no. 37, pp. 20345–20352, 2017.

[45] T. Y. Kim, S. Park, B. J. Kim et al., "Dual-functional quantum-dots light emitting diodes based on solution processable vanadium oxide hole injection layer," *Scientific Reports*, vol. 11, no. 1, p. 1700, 2021.

[46] H. Lindström, S. Södergren, A. Solbrand et al., "Li^+ ion insertion in TiO_2 (anatase). 2. Voltammetry on nanoporous films," *The Journal of Physical Chemistry B*, vol. 101, no. 39, pp. 7717–7722, 1997.

[47] J. Wang, J. Polleux, J. Lim, and B. Dunn, "Pseudocapacitive contributions to electrochemical energy storage in TiO_2 (anatase) nanoparticles," *The Journal of Physical Chemistry C*, vol. 111, no. 40, pp. 14925–14931, 2007.

[48] K. Kim and J.-H. Kim, "Bottom-up self-assembly of nano-netting cluster microspheres as high-performance lithium storage materials," *Journal of Materials Chemistry A*, vol. 6, no. 27, pp. 13321–13330, 2018.

[49] W. Weppner and R. A. Huggins, "Determination of the kinetic parameters of mixed-conducting electrodes and application to the system Li_3Sb," *Journal of The Electrochemical Society*, vol. 124, no. 10, p. 1569, 1977.

[50] Z. Shen, L. Cao, C. D. Rahn, and C.-Y. Wang, "Least squares galvanostatic intermittent titration technique (LS-GITT) for accurate solid phase diffusivity measurement," *Journal of The Electrochemical Society*, vol. 160, no. 10, article A1842, 2013.

[51] Y. Kim, S. C. Woo, C. S. Lee et al., "Electrochemical investigation on high-rate properties of graphene nanoplatelet-carbon nanotube hybrids for Li-ion capacitors," *Journal of Electroanalytical Chemistry*, vol. 863, article 114060, 2020.

[52] W. Ahn, D. U. Lee, G. Li et al., "Highly oriented graphene sponge electrode for ultra high energy density lithium ion hybrid capacitors," *ACS Applied Materials & Interfaces*, vol. 8, no. 38, pp. 25297–25305, 2016.